Optimizing Impedance Matching Parameters for Single-Frequency Capacitively Coupled Plasma via Machine Learning

Dehen Cao,[1] Shimin Yu,[2] Zili Chen,[2] Yu Wang,[1] Hongyu Wang,[3] Zhipeng Chen,[2] Wei Jiang,[1, 2] and Ya Zhang[4]
[1)]*School of Physics, Huazhong University of Science and Technology, Wuhan 430074, China*
[2)]*International Joint Research Laboratory of Magnetic Confinement Fusion and Plasma Physics, State Key Laboratory of Advanced Electromagnetic Engineering and Technology, School of Electrical and Electronic Engineering, Huazhong University of Science and Technology, Wuhan 430074, China*
[3)]*School of Physics Science and Technology, Anshan Normal University, Anshan 114000, China*
[4)]*Department of Physics, Wuhan University of Technology*

(*Corresponding authors: weijiang@hust.edu.cn and yazhang@whut.edu.cn)

(Dated: 19 July 2026)

Impedance matching plays a critical role in achieving stable and controllable plasma conditions in capacitive coupled plasma (CCP) systems. However, due to the complex circuit system, the nonlinear relationships between components, and the extensive parameter space of the matching network, finding optimal component values poses significant challenges. To address this, we employ an artificial neural network (ANN) as a surrogate model for the matching system, leveraging its powerful pattern learning capability for a reliable and efficient search for matching parameters. In this paper, we designed four different parameters as optimization objectives and took the modulus of the reflection coefficient as an example to demonstrate the impedance matching optimization process of a CCP in detail using a particle-in-cell/Monte Carlo collision (PIC/MCC) model. Our approach not only provides an effective optimization direction but also furnishes an entire parameter space that aligns with expectations, rather than just a single point. Moreover, the method presented in this paper is applicable to both numerical simulations and experimental matching parameter optimization.

I. INTRODUCTION

Capacitively Coupled Plasma (CCP) is a plasma generation technique that utilizes radio frequency (RF) energy to create and sustain a low-pressure gas plasma. It involves the application of an RF power supply to parallel electrodes separated by an insulating material, leading to plasma formation[1]. When an RF power supply is applied to the electrodes, an oscillating electric field is created between them. This electric field ionizes the gas molecules, creating a plasma. The electrons in the plasma are accelerated by the electric field, and they collide with other gas molecules, causing them to become ionized as well. This process creates a self-sustaining plasma, which continues to exist as long as the RF power supply is turned on. CCP has a wide range of applications, including plasma etching[2,3], plasma deposition[4], plasma cleaning[5], and plasma surface modification[6].

However, a significant challenge in CCP plasma generation is that the impedance of the plasma is not always matched to the impedance of the RF power supply. This can lead to power losses and inefficient plasma generation, or worse, reflections of RF power, which can damage the power supply[7]. To address this issue, impedance matching circuits are often utilized in CCP plasma systems; the goal of impedance matching is to maximize the power transferred from the RF power supply to the plasma by ensuring that the output impedance of the power supply matches the input impedance of the plasma load[8–10]. When the plasma impedance is matched to the impedance of the RF power supply, reflections of RF power can be reduced, which can help prevent damage to the power supply, CCP plasma generation can be stable and efficient, which can help improve the overall performance of the plasma system[11,12].

The impedance matching circuit is often achieved by placing an impedance matching network (IMN) between the generator and the plasma chamber (Fig. 1). IMN comes in different configurations such as L-type, T-type, and π-type[12–14]. Researchers have studied various techniques for designing effective IMNs and proposed several design approaches. In numerical simulation, Qu et al.[8] computationally modeled the full circuit and adjusted matchbox capacitors to achieve impedance matching to the time-varying plasma load during pulsed operation, but faced limitations from plasma simplifications and inherent mismatches. Zhang et al.[15] presented direct search extremum seeking by incrementally perturbing capacitor setpoints to reduce reflected power, and perturbation-based extremum seeking using sinusoidal dither signals, high-pass filters, and gradient estimation to optimize capacitors. Zhou et al.[16] use 3D Maxwell finite element modeling to simulate the impedance of an inductively coupled plasma driver with plasma represented as a uniform conductive medium, providing impedance data to design the matching network.

In experimental work, Parro et al.[7] presented a gradient-based automated impedance matching system for industrial microwave heating using adjustable waveguide posts and reflection magnitude feedback, but faced potential limitations in convergence speed and finding the global optimal solution. Vander et al.[17] describe an impedance matching method using a switched stub approach with plasma switching, where plasma cell switches are used to control the connection of stub branches to a main transmission line, allowing dynamic tunable matching by varying the states of the switches.

However, due to the complex plasma behavior and non-

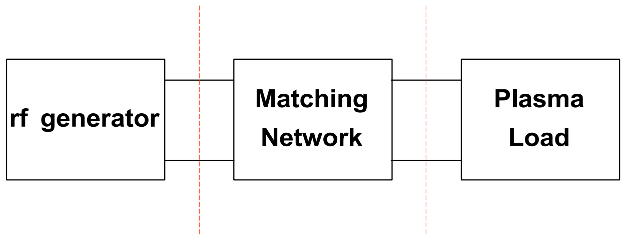

FIG. 1. The CCP structure with an impedance matching network added.

linear system dynamics, previous works have faced issues like low optimization efficiency or convergence to local rather than global optima[18–21]. In addition, one significant difficulty in impedance matching in CCP systems is the extensive parameter space of the matching network[22]. The matching network consists of various components such as capacitors, inductors, and transmission lines, each with multiple parameters that include values, sizes, and positions. Optimizing the impedance matching requires exploring this vast parameter space to find the right combination that minimizes the reflected power and maximizes power transfer efficiency. With numerous possible configurations, it becomes challenging to determine the optimal values for each component, often requiring iterative adjustments and extensive experimentation. The complex and large parameter space poses a significant challenge in achieving efficient impedance matching in CCP systems.

In order to address the above issues, recently Yu et al.[23] provided a possible best matching point through numerical iterations. The method achieves impedance matching for single-frequency CCP through an iterative, self-consistent coupling of particle-in-cell plasma simulations with external circuit models to minimize the reflection coefficient. However, in practical industrial settings, it may only be adjusted to a certain interval and cannot be accurately adjusted to that point. In addition, it is often more helpful to provide an optimization direction rather than just a single data point. Therefore, based on Yu's work, this paper proposes using an artificial neural network (ANN) as a surrogate model to effectively depict the matching performance. This approach allows us to demonstrate the direction of optimization during the optimization process and also provides a parameter space that meets the requirements.

ANN is a fundamental method used in machine learning. It relies on its powerful ability to fit functions, and it can learn and recognize patterns, relationships, and complex representations from input data. ANN excels at handling complex and high-dimensional data, so it offers a suitable solution for addressing the challenge of large parameter spaces and nonlinear behavior in impedance matching for CCP systems. By using ANN as the Surrogate model, it becomes possible to efficiently explore and optimize the parameter space, and the model can approximate the behavior of the system, allowing quick estimation of responses for different combinations of parameters.

ANN has been used extensively for parameter estimation and optimization, and this method has been proven effective in plasma-related applications[24–26]. Specifically, Shadmehr et al.[27] use neural networks to estimate process parameters in reactive ion etching. Hong et al.[28] present a neural network-based model for reactive ion etching using optical emission spectroscopy data. Himmel and May[29] discuss the advantages of neural networks over traditional statistical techniques in plasma etch modeling. Bleakie and Djurdjanovic[30] propose a multiple model system that uses neural networks to estimate the quality of the manufacturing process. Gergs et al.[31] employed neural networks to model aluminum film deposition processes. Wang et al.[32] trained deep neural networks on simulation data to predict discharge characteristics in CO_2 dielectric barrier discharges. Zhang et al.[33] also developed a deep neural network to efficiently predict discharge characteristics, such as current density, in discharges from the dielectric barrier of atmospheric pressure.

These papers demonstrate the successful utilization of neural networks and machine learning techniques in various plasma-related applications, validating their potential to optimize impedance matching parameters for a single-frequency CCP. The work described in this paper is to use ANN to accelerate the exploration process, reducing the need for time-consuming experimentation and enabling improved impedance matching in CCP systems. This paper is organized as follows: In Sec.II, we mainly introduced the numerical simulation methods of circuits and the fitting methods using ANN. In Sec. III, we provide a detailed demonstration of the optimization process and results using ANN with the reflectivity coefficient as the target. We also compare these results with those obtained for three other target parameters. The conclusion is presented in Sec.IV.

II. METHOD

The content of this section is arranged as follows: Sec. II A introduces the circuit structure and the relevant parameters used for numerical simulations. Sec. II B presents four metrics we have defined to measure matching performance, which will be used as optimization objectives for the subsequent optimization of ANN. Sec. II C explains how this study utilizes ANN as a surrogate model and describes the iterative optimization process.

A. Analog circuit settings

A common circuit structure was selected for simulation, as shown in Fig. 2. The whole system was divided into three parts: radio frequency generator (RF), impedance matching network (IMN) and plasma load. In the plasma circuit, the RF generator is the source of RF power for the CCP, producing a sinusoidal signal within the frequency range of a few MHz to a few GHz. Its power output can be adjusted to regulate the plasma's intensity. To ensure efficient power transfer, the IMN comes into play, harmonizing the impedance of the RF generator with that of the plasma load. This network typically

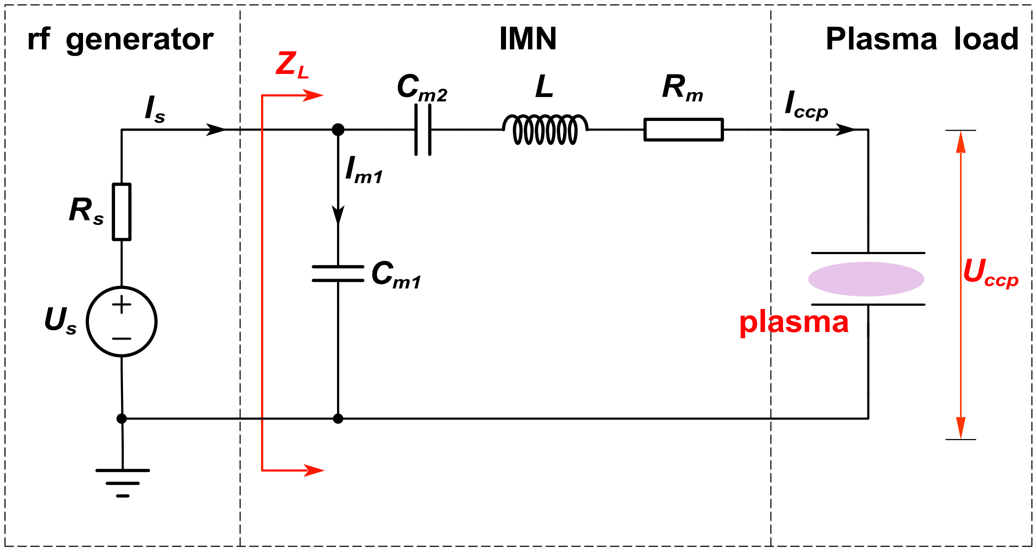

FIG. 2. The network of plasma coupled circuit that is simulated. The first part is the radio frequency generator. The second part is the impedance matching network. The third part is the plasma load. C_{m1}, C_{m2}, and L are the matching parameters that we need to design.

consists of capacitors and inductors. The plasma load, in turn, absorbs the RF power, enabling the creation of plasma. Typically, the plasma load comprises a gas that undergoes ionization as a result of the RF power, forming a plasma state characterized by a significant concentration of free electrons.

Here are the detailed parameter information for these components:

- RF generator: The 13.56 MHz source was used in the simulations, with internal impedance R_s of 50 Ω and fixed power of 20 W.
- Impedance Matching Network(IMN): The IMN is an L-type topology consisting of two capacitors: one inductor and one equivalent loss resistance of the IMN. The C_{m1}, C_{m2}, and L are the parameters to be adjusted.
- Plasma load: A 1D implicit particle in cell / Monte Carlo collision (PIC-MCC)[34–38] algorithm was used to simulate single-frequency CCPs. The distance between the electrodes was 0.03 m. The working gas was argon, with the gas pressure and temperature of 100 mTorr and 300 K, respectively. The space step was set at 4.6875×10^{-4} m. The simulation time step was set to 1.0×10^{-10} s.

Regarding the PIC/MCC model being used here, the following points need to be noted:

- At low pressures (less than 10 Pa), metastables were thought to have little effect on ionization in the plasma bulk itself, since studies found that direct ionization from the ground state dominated at such pressures[39–41]. Additionally, tracking metastable particles in PIC/MCC simulations requires high computational costs. Therefore, in most current particle-based modeling studies, excited-state atoms with relatively low density are excluded[42,43]. We also do not consider metastable particles here.
- The MCC model accounts for three types of electron-neutral collisions (elastic, excitation, and ionization) and two types of ion-neutral collisions (elastic scattering and charge exchange). Neutral particles are assumed to be stationary and uniformly distributed, as their total ionization degree is less than 0.01%. The simulation accounts for ionization and excitation collisions of electrons with Ar atoms and elastic collisions of electrons and Ar^+ ions with Ar atoms. These collisions are simulated using a series of random numbers and collision cross sections, which are downloaded from the widely used LXCat database[44–48].

Note that the parameter values mentioned above are the same as those in Yu's work[23], so we can compare them with previous results.

B. Optimization objectives

In order to evaluate the effectiveness of the match, we sequentially selected the following four parameters to measure the performance of the match as optimization objectives, and Table I summarizes the advantages and disadvantages of these four optimization objectives.

1. The modulus of the reflection coefficient, $|\Gamma|$

The reflection coefficient, Γ, is commonly used in industry to measure the matching performance between intercon-

TABLE I. Comparison of optimization objectives for impedance matching.

Optimization Objectives	Description	Advantages	Disadvantages
$\lvert\Gamma\rvert$	The modulus of the reflection coefficient.	Industry standard metric for measuring impedance mismatch	Only considers modulus, not phase
D_{cs}	Similarity between power impedance and IMN impedance.	Considers both modulus and phase	More complex calculation and less intuitive than reflection coefficient
η	The power absorption efficiency of the plasma load.	Key indicator of impedance matching performance	Requires integration over RF cycle; does not provide impedance information
U_{ccp}	Voltage across the plasma load at both ends.	Simple direct measurement; important for many plasma processes	Does not directly indicate impedance matching; voltage alone does not fully characterize plasma

nected components. It provides engineers with valuable information about the level of impedance mismatch, which directly affects signal integrity, power transfer efficiency, and overall system performance. By analyzing the reflection coefficient, engineers can optimize the design and performance of various systems, such as RF circuits, antennas, transmission lines, and audio systems.

The reflection coefficient has several characteristics:

- It is generally a complex number[15]. Because the reflection coefficient is obtained from Eq.1, where Z_L is the load impedance, and Z_0 is the characteristic impedance of the transmission line or system, the impedance in this equation is a complex number consisting of the resistance of the real part and the reactance of the imaginary part, so the reflection coefficient obtained is naturally a complex number.

$$\Gamma = \frac{Z_L - Z_0}{Z_L + Z_0} \tag{1}$$

- The modulus of the reflection coefficient, $|\Gamma|$, represents the fraction of the incident power that is reflected. The modulus of the reflection coefficient can be anywhere from 0 to 1. A modulus of 0 means that no power is reflected, while a modulus of 1 means that all the power is reflected.

- The angle of the reflection coefficient, θ, represents the phase difference between the reflected and incident waves. The angle of the reflection coefficient can range from 0 to 360 degrees. A phase difference of 0 degrees means that the reflected wave is in phase with the incident wave, while a phase difference of 180 degrees means that the reflected wave is 180 degrees out of phase with the incident wave.

In this paper, Z_0 refers to the output impedance of the RF source, denoted as Z_S. That is, the calculation equation for Γ in this paper is

$$\Gamma = \frac{Z_L - Z_S}{Z_L + Z_S}. \tag{2}$$

And in order to quantitatively measure the degree of matching between the plasma load and the power supply, reference to Yu's work[23], we use the modulus of the reflection coefficient, $|\Gamma|$, to be one of the measurement criteria.

2. Impedance similarity, D_{cs}

As mentioned above, the reflection coefficient is a complex number, and when delivering AC power to complex load impedances, the maximum real power is delivered to the load when the impedance of the source is equal to the complex conjugate of the load impedance[49]. Therefore, when evaluating the matching performance, only considering the modulus of the impedance is not sufficient. Therefore, we introduced the parameter "impedance similarity", denoted D_{cs}, to simultaneously characterize the matching of both the modulus and phase angle.

The calculation method for this parameter is as follows:

$$D_{cs} = \frac{\vec{a}\cdot\vec{b}}{||\vec{a}|| * ||\vec{b}||} * \frac{\min(||\vec{a}||, ||\vec{b}||)}{\max(||\vec{a}||, ||\vec{b}||)}, \tag{3}$$

where

$$\vec{a} = (R_L, X_L),\ \vec{b} = (R_s, X_s), \tag{4}$$

R_L and X_L are the real and imaginary parts of the input impedance of the matching network, R_s and X_s are the real and imaginary parts of the output impedance of the RF source.

In Eq.3, the first term is to calculate the similarity between two vectors. Cosine similarity is a metric used to measure the similarity between two vectors in a vector space. It is widely used in information retrieval, text mining, and recommendation systems. The cosine similarity is based on the concept of cosine of the angle between two vectors. Given two vectors, $\vec{A}$ and $\vec{B}$, the cosine similarity (S_C) between them is calculated using the following formula:

$$S_C(\vec{A}, \vec{B}) = \frac{\vec{A}\cdot\vec{B}}{||\vec{A}|| * ||\vec{B}||}, \tag{5}$$

where $\vec{A} \cdot \vec{B}$ represents the dot product of vectors $\vec{A}$ and $\vec{B}$, and $||\vec{A}||$ and $||\vec{B}||$ denote the magnitudes (or norms) of the vectors. The resulting value of cosine similarity ranges from -1 to 1. A value of 1 indicates that the vectors are identical, 0 indicates that the vectors are orthogonal (i.e., not similar), and -1 indicates that the vectors are diametrically opposed.

The second term in Eq.3 represents a penalty term when the magnitudes of two vectors are not equal. When the magnitudes of the two vectors are similar, the value of this term tends to be 1. When the magnitudes differ significantly, the value of this term tends to be 0.

So, based on the above statements, we can see that "D_{cs} = cosine similarity * modulus penalty term". When the magnitudes and angles of the two vectors are similar, the value of D_{cs} tends to be 1. Additionally, when the magnitudes are nearly identical, this parameter degenerates into cosine similarity.

3. Power absorption efficiency, η

The power absorption efficiency of the plasma load, which refers to the ratio of the active power of the plasma load to the active power of the power supply, denoted as η. The power absorption efficiency of the plasma is a measure of how much of the RF power is actually absorbed by the plasma. This efficiency can be used to measure the impedance matching performance of the CCP. A high power absorption efficiency indicates that the impedance of the plasma is well matched to the impedance of the RF source, and vice versa[8,50].

It can be calculated using the following method:

$$\eta = \frac{\overline{P_{ccp}}}{\overline{P_s}} = \frac{(\sum_{i=nRun-N}^{nRun} P_{ccp(i)})/N}{(\sum_{i=nRun-N}^{nRun} P_{s(i)})/N}. \tag{6}$$

Here, the variable $nRun$ represents the total number of radio frequency cycles and N represents the number of cycles considered after reaching steady state, $P_{ccp(i)}$ and $P_{s(i)}$, respectively, represent the active power of the plasma load and the power supply during the $i-th$ radio frequency cycle, and their calculation methods are as follows:

$$P_{ccp(i)} = \frac{\int_0^{T_{rf(i)}/2} U_{ccp}(t) I_{ccp}(t)dt}{T_{rf(i)}/2} \tag{7}$$

and

$$P_{s(i)} = \frac{\int_0^{T_{rf(i)}/2} U_s(t) I_s(t)dt}{T_{rf(i)}/2}, \tag{8}$$

where $T_{rf(i)}$ is the $i-th$ RF cycle, U_{ccp} and I_{ccp} are the instantaneous voltage and current across the CCP load, respectively. U_s and I_s are the instantaneous voltage and current of the radio frequency power supply, respectively. Because the frequency doubles when the voltage and current are multiplied, only half of the RF cycle should be integrated.

4. Plasma load voltage, U_{ccp}

Voltage across the plasma load at both ends, which refers to the U_{ccp} in Fig. 2.

In many applications of CCP, it is necessary not only to achieve high plasma density but also to achieve high plasma loading voltage to produce more energetic ions or create a more uniform plasma. For example, in thin film deposition, high voltage enhances the energy of plasma species, resulting in improved film adhesion and uniformity[51]. In plasma etching, higher voltages accelerate the ion energy, allowing more efficient material removal[52]. Furthermore, plasma surface modification and sterilization processes benefit from high CCP load voltages by promoting surface activation, chemical reactions, and the generation of reactive species[53].

In addition, compared to the parameters mentioned above, the voltage across the two ends of the CCP load is a simpler quantity that can be directly measured. It should be noted that here we take the value of U_{ccp} when the CCP reaches a stable state.

C. Optimization methods

The working method of this paper is to treat the entire circuit model as a black box, as shown in Fig. 3, we input the matching parameters into the black box and obtain the relevant target variables. We don't focus on the specific details of the circuit or the interactions between its various components. Instead, we only care about the circuit parameters we can change and the corresponding effects we can achieve.

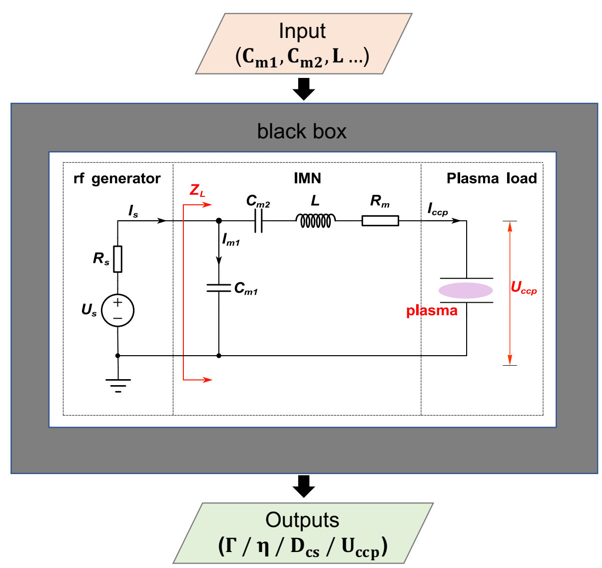

FIG. 3. Black box model for impedance matching optimization. The entire circuit is treated as a black box function, with matching parameters as inputs and the target variable, which measures the matching performance, as the output.

In general, the black box model can be described by the following equation:

$$y = f(x_1, x_2, \ldots), \tag{9}$$

where y is the variable measuring the matching performance and x_i represents the matching parameters of the circuit. Then we use an ANN to fit this function, thereby transforming the search problem for matching parameters into a function optimization problem.

In this paper, the form of Eq. (9) is $y = f(C_{m1}, C_{m2}, L)$, where C_{m1}, C_{m2}, and L are the matching parameters in Fig. 2. And for the convenience of visualizing the results, we fixed the value of C_{m2} to $200pF$ and only explored the impact of C_{m1} and L on the matching performance. That is, the actual fitting equation is the following:

$$y = f(C_{m1}, L). \tag{10}$$

Fig. 4 shows the workflow for determining the optimal matching parameters and their corresponding ranges. Initially, we construct a comprehensive parameter space, denoted A_i, consisting of grids spaced at intervals of S_i. Subsequently, we input the parameters located on the grid points into the simulation program to obtain the corresponding target variable, y. Using the acquired data, we train a neural network model to fit the function $y = f(C_{m1}, L)$ and utilize this model to predict both the optimal matching parameter P_i, and the next parameter space more accurate and refined A_{i+1}. We then reload the parameter P_i into the simulation program and assess its matching performance. If the performance meets our expectations, we output the parameter. However, if the performance falls short of expectations, we reduce the parameter space and repeat the process.

Referring to the work of Bonzanini et al.[24], we use fully connected networks to fit Eq. (10), the architecture of the networks is shown in Fig. 5. We input C_{m1} and L into the neural network and output the predicted values of the corresponding target variable ($|\Gamma|$ or D_{cs} or η or U_{ccp}).

The neural network architecture employs an identical number of nodes in each layer, with the specific value of the nodes determined using the Bayesian optimization algorithm. The activation function is fixed as the tanh function, and for each model, a fixed number of 10000 iterations are executed. Due to the limited size of the available data, the batch_size is set to the length of the entire data set. The other hyperparameters of the ANN, including the number of nodes per layer and the learning rate, are also optimized through the Bayesian optimization algorithm, as illustrated in Fig. 6. To facilitate this optimization process, we used the library available on GitHub[54]. This library provides the necessary tools and functionalities for implementing the Bayesian optimization algorithm and effectively fine-tuning the ANN hyperparameters, which ultimately enhances the model's performance and generalization capabilities.

Fig. 6 shows the comprehensive workflow employed to harness Bayesian optimization in the selection of optimal hyperparameters for ANN models. To facilitate the generation of robust and more accurate models, we performed the following pre-processing steps on the raw data. Our approach involved a series of essential steps aimed at enhancing the performance of the models. The initial step was to randomly shuffle the data, which played a crucial role in eliminating any inherent biases or patterns that might have existed in the raw data. By doing so, we aimed to create a more diverse and representative dataset that would allow the model to learn from various scenarios and generalize better to unseen data. The next critical stage involved data normalization. This process brought all data points into a standardized range, which was particularly beneficial for certain machine learning algorithms, including neural networks. Normalization ensured that each feature in the data set had a comparable scale, preventing any specific feature from dominating the model's learning process due to its large magnitude. This step significantly improved the model's convergence, enabling it to find optimal solutions more efficiently during the training phase. Subsequently, we focused on partitioning the entire dataset into five distinct subsets, each containing an equal representation of data instances. This technique, known as cross-validation, played a pivotal role in assessing the model's performance and generalization capabilities. By training the model on four of the subsets and validating it on the fifth one in a cyclical manner, we could identify potential overfitting and assess the model's ability to handle unseen data effectively.

The ensuing step entails the execution of a meticulous five-fold cross-validation procedure, wherein the ANN model is trained on each of the five subsets separately. This process culminates in the calculation of the average Mean Squared Error (MSE) as a performance metric. Herein, our primary objective is to meet specific expectations concerning the MSE value obtained. Should the resulting MSE satisfy our predefined expectations, the corresponding hyperparameter combination is dutifully extracted and subsequently utilized to train the entire dataset. However, in the event that the achieved MSE value fails to meet the desired expectations, a more sophisticated approach is adopted. Here, we invoke the potent Bayesian optimization algorithm to dynamically adjust and optimize the hyperparameter combination, based on the information learned from previous iterations. The Bayesian optimization algorithm, known for its efficiency in optimizing expensive and nonconvex functions, guides the process towards identifying improved hyperparameters that better align with the desired performance criteria.

Following the Bayesian optimization-guided hyperparameter update, a fresh round of 5-fold cross-validation is initiated, allowing the ANN model to be retrained on the data subsets using the refined hyperparameter combination. This iterative process continues until the MSE value finally aligns with the predefined expectations, signaling the convergence of the hyperparameters to an optimal configuration.

The integrative interplay between the Bayesian optimization algorithm and the 5-fold cross-validation training technique ensures that the most suitable hyperparameters are ascertained to maximize the ANN model's performance on the dataset. This systematic and data-driven approach offers an efficient and effective methodology for hyperparameter tuning, thereby bolstering the overall efficiency and accuracy of the Artificial Neural Network model.

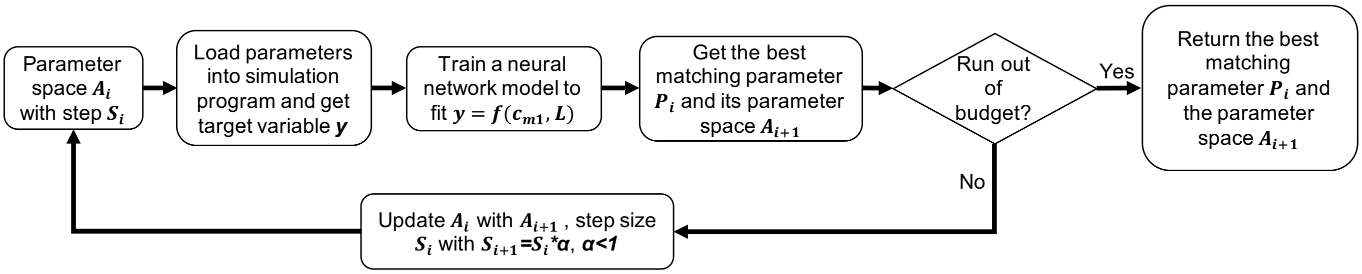

FIG. 4. Workflow of the machine learning approach for finding the best matching parameters iteratively.

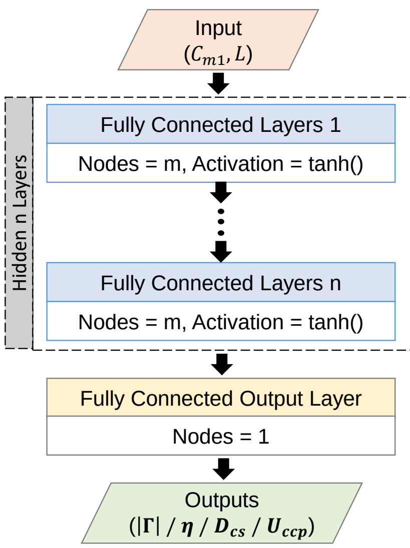

FIG. 5. Architecture of the artificial neural network trained to predict the target variable for measuring matching effectiveness. The neural network has n hidden layers and each layer has the same number of m nodes. The activation function used in each hidden layer is the same and fixed to tanh().

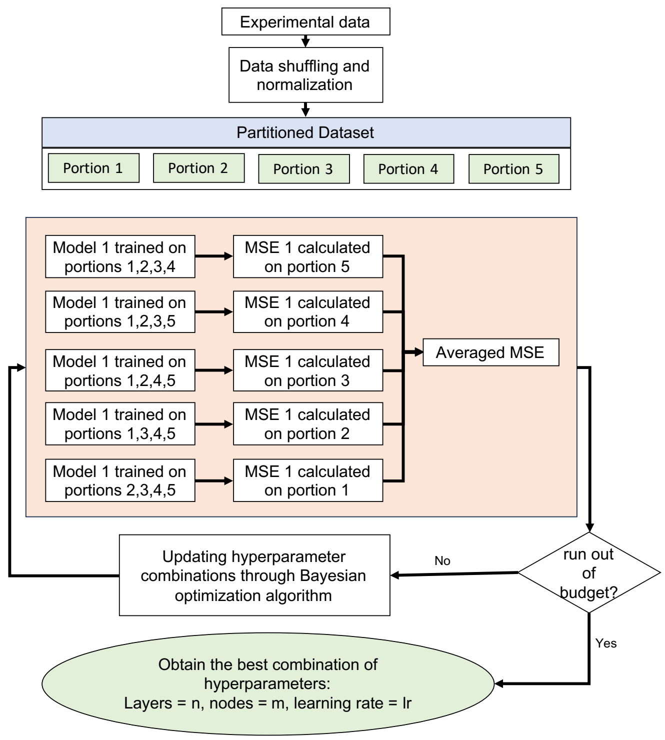

FIG. 6. The workflow for automatically obtaining hyperparameter combinations of artificial neural network models. The workflow consists of learning the weights and biases of the artificial neural network model via 5-fold cross-validation and active learning of the hyperparameters of the neural network model.

In summary, our method is to use Bayesian optimization algorithm and 5-fold cross-validation to find the best ANN model hyperparameters and then use the model to fit the original data to obtain the distribution of the target variable in the full parameter space. It is important to note that after selecting the best ANN hyperparameter combination shown in Fig. 6, we used all the original data for model training.

III. RESULT

The main content of this section is as follows: Using the methods mentioned above, in Sec. III A, we extensively discuss the optimization process and results with the reflection coefficient as the objective. In Seq. III B, we present the optimization results with three other parameters (D_{cs}, η, U_{ccp}) as objectives and provide a detailed comparison of the four optimization results.

A. Reflection coefficient as optimization objective

In this section, we demonstrate the optimization process in detail using the reflection coefficient as the optimization objective. Section III A 1 shows the process of iteratively refining the parameter space to finally obtain an ideal parameter region. The goal is to explain how we accomplish the selection and optimization of parameter regions and the rationale behind our optimization choices. Since our aim is not only to find the optimal parameter point, but more importantly to identify a parameter region that meets the expected requirements, in Section III A 2, we randomly select points in different value ranges in the final parameter space and compare their matching performance. The proximity of matching effects for different points within the same region demonstrates that the optimized region can indeed provide solutions that satisfy the parameter range, rather than just a single optimal point. This will have a very positive impact on industrial parameter tuning.

1. Optimization process

Table II shows the parameter spaces we have scanned sequentially, where A_0 represents the parameter space we scanned in the first round. A_1 is the next optimization region selected based on the results obtained from A_0, and it is acquired dynamically. Similarly, A_2 is optimized based on A_1.

The progressive optimization process of the parameter space is as follows: In space A_0, the value of C_{m1} starts at 50 pF, ends at 1000 pF, with a step size of $50pF$. The value of L starts at 4.0 μH, ends at 9.0 μH, with a step size of 0.5 μH. By dividing C_{m1} and L, a parameter space with a horizontal axis of C_{m1} and a vertical axis of L was obtained, containing a total of 220 combination points, then we load these points into the simulation program and obtain the reflection coefficients corresponding to each set of parameters. Next, we used these 220 sets of data to train the ANN. ANN hyperparameters were obtained using the Bayesian optimization algorithm depicted in Fig. 6, when the 5-fold cross-validation error reaches the expected level, the fitting of the ANN to Eq.11 is completed. Furthermore, we can use this trained model to provide values of the reflection coefficient throughout the parameter space, essentially continuously rather than only on the parameter grid, as shown in Fig. 7(a), the ANN hyperparameters corresponding to it are also shown in Table II as A_0.

$$|\Gamma| = f(C_{m1}, L) \tag{11}$$

In Figure 7(a), the ANN model indicates that the minimum reflection coefficient point occurs at the point $(cm1, L) = (452.167\text{ pF}, 5.417\ \mu\text{H})$, which is approximately in the region $A_1 = \{C_{m1} \in (200\text{ pF}, 500\text{ pF})\} \cap \{L \in (5.4\ \mu\text{H}, 5.9\ \mu\text{H})\}$. The MSE of the model corresponding to this point in Table II(A_0) is 0.0031, which seems to be a relatively accurate and good result. However, it is also easy to see that there is a wide range of unstable regions in the parameter space, indicating that the training set we actually used is much smaller than the data set we scanned. This has a certain impact on the accuracy of the ANN model. Moreover, the existence of potential saddle points also requires us to shrink the parameter space and perform a more fine-grained scan to exclude the influence of unstable regions, improve accuracy, and reliability. Therefore, we are conducting a new round of scanning in the new parameter space, and the specific parameter settings are shown in A_1 in Table II.

In Fig. 7(a), we need to pay special attention to the following points: First, the shaded areas in the figure are areas where oscillations occur, which is an unstable discharge mode caused by periodic breakdown of the CCP. In this particular mode, the plasma experiences erratic fluctuations, which makes the simulation data derived from these regions unreliable and inaccurate. Therefore, during data preprocessing, we labeled the oscillatory data and trained a classification model to identify the oscillation regions within the entire parameter space. Using this classification model, we were able to isolate and recognize these unstable regions, commonly characterized by oscillations. Subsequently, we used shadowing to mask these regions and avoided using data from these regions during training with the reflectance coefficient as the target. By avoiding the use of data from oscillation regions during training, the model was rendered more robust and capable of providing accurate predictions. Secondly, we did not impose any range restrictions on the output results of the ANN. Our objective is to find the minimum point, so even if the ANN predicts results greater than 1 or less than 0 at certain positions, it does not affect our search for the relative minimum value. The flexibility of the output range of neural networks allows us to focus on locating the minimum point, and the size of the output beyond the reasonable range can also reflect the accuracy of the model to some extent.

The new discharge mode mentioned above mainly manifests as significant periodic oscillations when certain components in the circuit reach specific values. Parameters such as the voltage across the plasma load, current in the corresponding branch, plasma load power, electron density between plates, and electron temperature all exhibit substantial periodic oscillations. Furthermore, the frequency of the oscillation is influenced by factors such as power supply voltage, power supply frequency, component parameters of the matching network, CCP's plate area, and plate gap. When such oscillations occur, the obtained values of reflection coefficients and the like are not accurate, so we need to avoid entering the corresponding parameter space (shadowed area). The analysis of this discharge mode is beyond the scope of this paper, so we will discuss it in detail in a future paper.

Fig. 7(b) shows the distribution of reflection coefficients corresponding to the parameter space A_1, for the same reason as in A_0, we have obtained a third parameter space A_2. And after applying the same "parameter grid - simulation program - BO hyperparameter selection - ANN fitting" process to A_2, we obtained the distribution of reflection coefficients on A_2 as shown in Fig. 7(c).

Fig. 7(c) shows that the unstable region occupies only a small part of the new parameter space, which to some extent indicates that this is a relatively good region. Additionally, Fig. 7(c) shows that when the matching parameters (C_{m1}, L) are set to $(469.444\text{ pF}, 5.495\ \mu\text{H})$, we obtain the minimum reflection coefficient. Notably, Fig. 7(c) exhibits multiple nearby saddle points, implying that similar matching performance could be achieved in different areas. Furthermore, we randomly marked a point in each of the different value ranges in Fig. 7(c). These points will be used to compare the matching effects of the parameter values in different regions, which we will introduce in detail later.

Up to this point, the process of optimizing with the reflection coefficient as the objective has concluded. We have obtained three continuously refined parameter spaces as shown in Fig. 7, along with their corresponding best-matching pa-

TABLE II. Parameter space and corresponding hyperparameters of ANN models. C_{m1}, C_{m2} and L represent the matching parameters in Fig. 2, Hidden layers, Nodes, and Learning rate are the hyper parameters of ANN model fitting the corresponding parameter space data. MSE is the mean squared error between the model's predicted data and the original data.

name	$C_{m1}(pF)$[a]	$C_{m2}(pF)$	$L(\mu H)$	Hidden layers	Nodes	Learning rate	MSE
A_0	[50-1000-50]	200	[4.0-9.0-0.5]	4	21	0.003256	0.0031
A_1	[200-500-10]	200	[5.4-5.9-0.05]	7	20	0.000246	0.0017
A_2	[400-500-5]	200	[5.45-5.55-0.01]	3	19	0.001503	0.0011

[a] [A-B-C] indicates that the parameter starts at A and ends at B, with an interval of C between each step

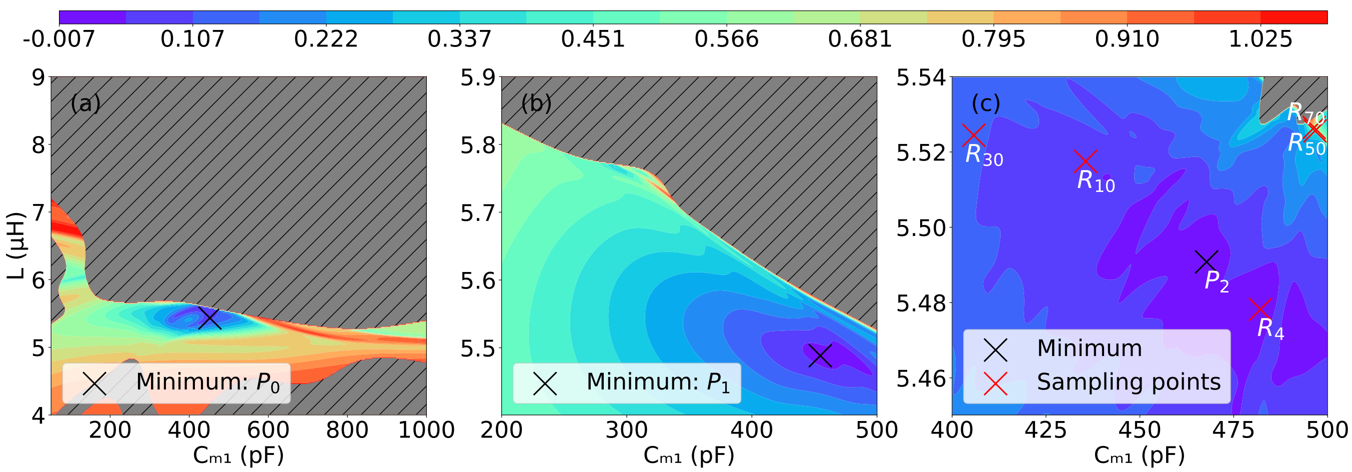

FIG. 7. The distribution of reflection coefficients values given by the neural network. The horizontal coordinate represents the capacitance C_{m1} in the IMN, and the vertical coordinate represents the inductance L. The shaded area represents the oscillation region, which is a new discharge mode we have discovered. We will discuss this discharge mode in subsequent papers. (a) The parameter space is A_0. The black cross indicates that the best parameter combination predicted by the neural network is $P_0(C_{m1}, L) = (452.167\ \mathrm{pF}, 5.417\ \mu\mathrm{H})$. (b) The parameter space is A_1. The best predicted parameter combination is $P_1(C_{m1}, L) = (454.667\ \mathrm{pF}, 5.488\ \mu\mathrm{H})$. (c) The parameter space is A_2. Black cross: The best-predicted parameter point is $P_2(C_{m1}, L) = (469.444\ \mathrm{pF}, 5.495\ \mu\mathrm{H})$. Red crosses: Points within different contour regions.

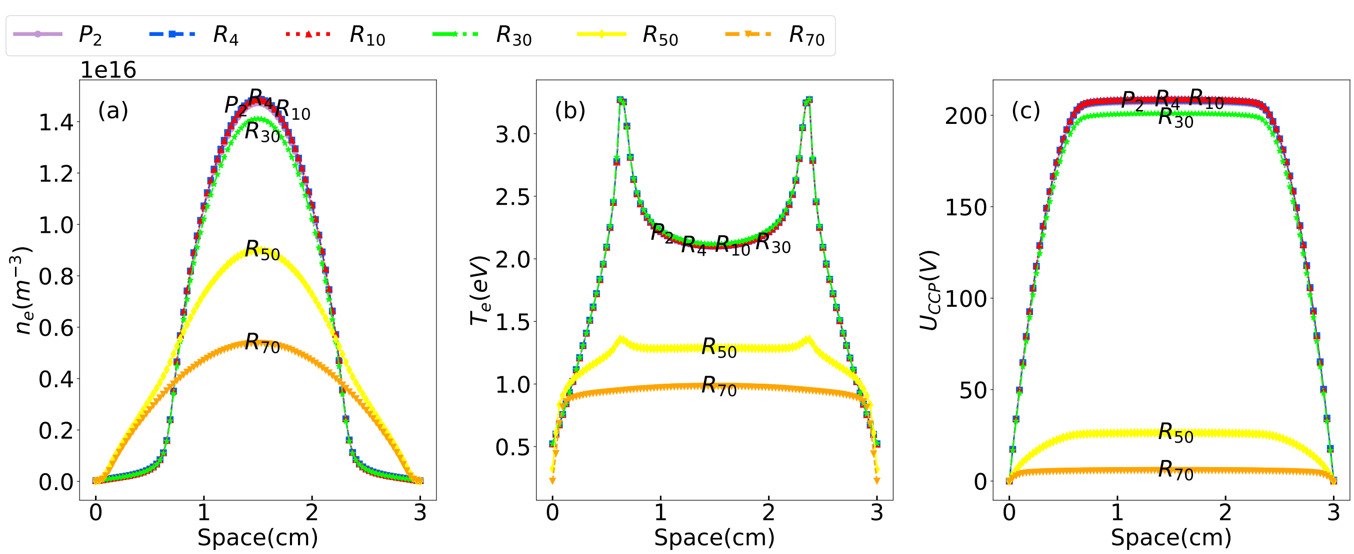

FIG. 8. Comparison of the matching performance between different sampling points. (a) Electron density. (b) Electron temperature. (c) Potential distribution. The horizontal axis represents the discharge gap, while the vertical axis represents the average values of the last 200 cycles after the CCP reaches a steady state.

rameters predicted by the ANN. Next, we will conduct a further analysis and discussion on these results.

2. Comparison of parameters across different value domains

To demonstrate the matching performance of the parameters in different regions of the entire parameter space, we selected several sampling points within different contour regions in Fig. 7(c). Points marked with black crosses represent the locations where the ANN predicts the minimum modulus of the reflectance coefficient, called the point P_2. The red crosses indicate sampling points within different contour regions. Here, R_4 signifies that a point is located in an area where the value is greater than the minimum by 0% to 4%, R_{10} corresponds to 6% to 10%, R_{30} corresponds to 20% to 30%, R_{50} corresponds to 40% to 50%, and R_{70} corresponds to 60% to 70%. The reason we avoid selecting adjacent contour regions is that the points obtained from neighboring areas might exhibit very similar matching performance, making it less convenient to showcase the distinctions between different regions. Additionally, since most of the data are concentrated within a region that does not exceed 10% above the minimum value, our points do not cover areas greater than 70%.

Fig. 8 illustrates a comparison of the matching performance of parameter points distributed across different value ranges. From the figure, as the value of the parameter $|\Gamma|$ decreases, the matching performance of the parameters in the simulation program continuously improves. This is evident in the significant increase in electron density after reaching a steady state and in the voltage at both ends of the CCP. Furthermore, when the value of $|\Gamma|$ is in a region below a certain threshold (such as the lowest 10%), the performance of the parameters in this region becomes consistent and reaches a relatively high level of matching performance. This observation is of significant practical importance in industrial operations. It implies that fine-tuning parameters to achieve a single, specific point within the parameter space is not essential. Instead, reaching a certain region within the parameter space is sufficient to achieve the desired outcomes. This insight can streamline the optimization process in industrial applications, as operators do not need to precisely adjust parameters to target a specific point, which could be time-consuming and challenging.

Furthermore, the consistent parameter performance within the identified region highlights the robustness and stability of the system. Even if the specific parameter values vary slightly due to inherent uncertainties or fluctuations in the operating conditions, the overall performance remains reliable and satisfactory. This robustness in the face of variations is crucial for industrial applications where maintaining stable and predictable outcomes is critical.

B. Other target optimization parameters

Before analyzing the results, let's consider the following question: Under what circumstances can we consider a set of parameters to be a better matching configuration? As mentioned in Sec. I, the goal of impedance matching is to maximize the power transferred from the RF power source to the plasma by ensuring the output impedance of the power source matches the input impedance of the plasma load, while minimizing the reflection of RF power from the plasma load. Therefore, theoretically, if a set of parameters corresponds to higher absorption efficiency and lower reflection coefficient, we consider those parameters to be a better set of matching parameters.

In Sec. III A, we achieved a well-performing parameter region through continuous optimization of parameter $|\Gamma|$. In this section, we will demonstrate the optimized parameter regions for the objectives mentioned in Sec. II B, namely η, U_{ccp}, and D_{cs}, using the same optimization approach. Furthermore, by comparing the results obtained from different optimization objectives, we will provide recommendations on how to choose optimization objectives in practical industrial production.

After an optimization process similar to the gradual reduction of the parameter space in Sect.III A, we obtained the final parameter space corresponding to η, U_{ccp}, and D_{cs}, as shown in Table III. It can be seen that η and U_{ccp} eventually converge to the same region, while $|\Gamma|$ and D_{cs} also converge to the same region. This indicates that there is a positive linear relationship between these parameters. Fig. 9 shows the results of using ANN to fit the values in the spaces mentioned in the aforementioned sequentially. It can be observed that saddle regions of varying sizes appear in the fitting graphs corresponding to different optimization objectives.

Fig. 10 shows a comparison of plasma parameters for different optimization objectives, and the detailed values are summarized in Table IV, Table V and Table VI. Table IV shows the best matching parameter points obtained under each of the four optimization objectives in this paper, as well as the best matching parameter point obtained by Yu in his paper[23]. However, since the point given by Yu is in the area of oscillation, we only compare the performance of the four sets of parameters in the following table. Table V shows the specific values of the optimization parameters corresponding to different optimization targets. For example, the first row indicates the specific values of absorption efficiency, plasma load voltage, impedance similarity, and modulus of reflection coefficient obtained when the optimization objective is set to absorption efficiency. Table VI shows the specific values of the plasma parameters and circuit parameters corresponding to different optimization targets. For example, the first row represents the specific values of the electron density in the middle of the electrode, the electron temperature, the power output from the power source, the power dissipated in the impedance matching network, and the power absorbed by the plasma load when the optimization objective is set to absorption efficiency. In addition, we use feedback control as shown in Eq.12 to regulate the power of the power supply. Therefore, it is normal for the curve in Fig. 10 to have small fluctuations. Unlike the oscillatory discharge mode mentioned earlier, the latter exhibits significant periodic oscillations in parameters

TABLE III. The parameter spaces corresponding to η, U_{ccp}, D_{cs} and $|\Gamma|$, as well as the hyperparameters of the ANNs fitted to each parameter space. C_{m1}, C_{m2} and L represent the matching parameters in Fig. 2, Hidden layers, Nodes and Learning rate are the hyper parameters of ANN model fitting the corresponding parameter space data. MSE is the mean squared error between the model's predicted data and the original data.

name	C_{m1}(pF)[a]	C_{m2}(pF)	L(μH)	Hidden layers	Nodes	Learning rate	MSE
η	[275-305-1]	200	[5.710-5.732-0.005]	4	45	0.003321	0.0060
U_{ccp}	[275-305-1]	200	[5.710-5.732-0.005]	6	38	0.001880	0.0107
D_{cs}	[400-500-5]	200	[5.45-5.55-0.01]	3	27	0.001105	0.0028
$\|\Gamma\|$	[400-500-5]	200	[5.45-5.55-0.01]	3	19	0.001503	0.0011

[a] [A-B-C] indicates that the parameter starts at A and ends at B, with an interval of C between each step

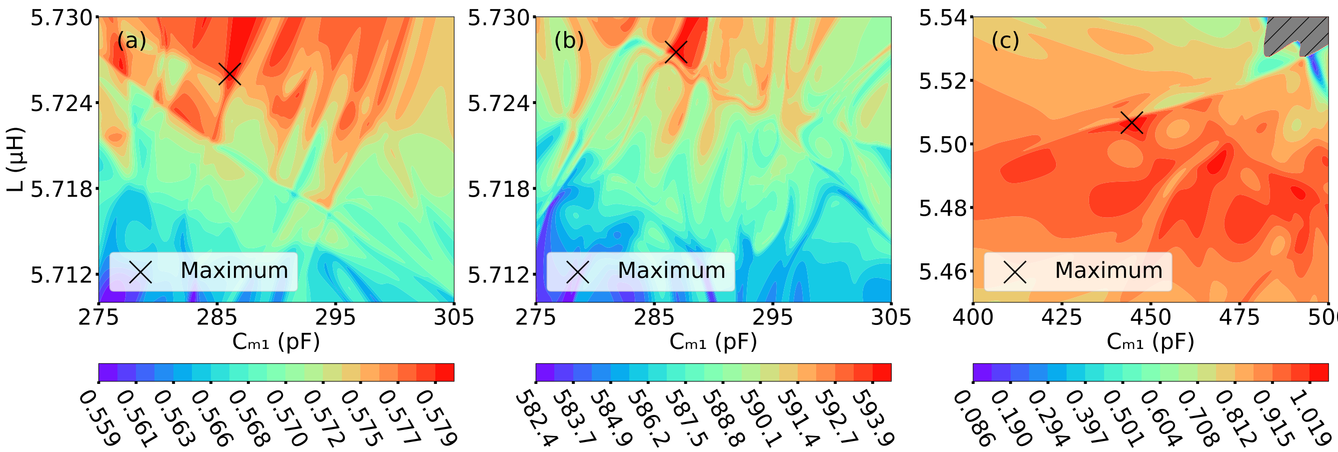

FIG. 9. The distribution of target parameters given by neural networks in their respective parameter spaces. (a)The plasmas power absorption efficiency as η. (b)The magnitude of plasma load voltage as U_{ccp}. (c)The similarity values between the impedance of the matching network and the impedance of the RF source as D_{cs}. The black cross is the best matching parameter combination predicted by the neural network, and its specific values are listed in Table IV.

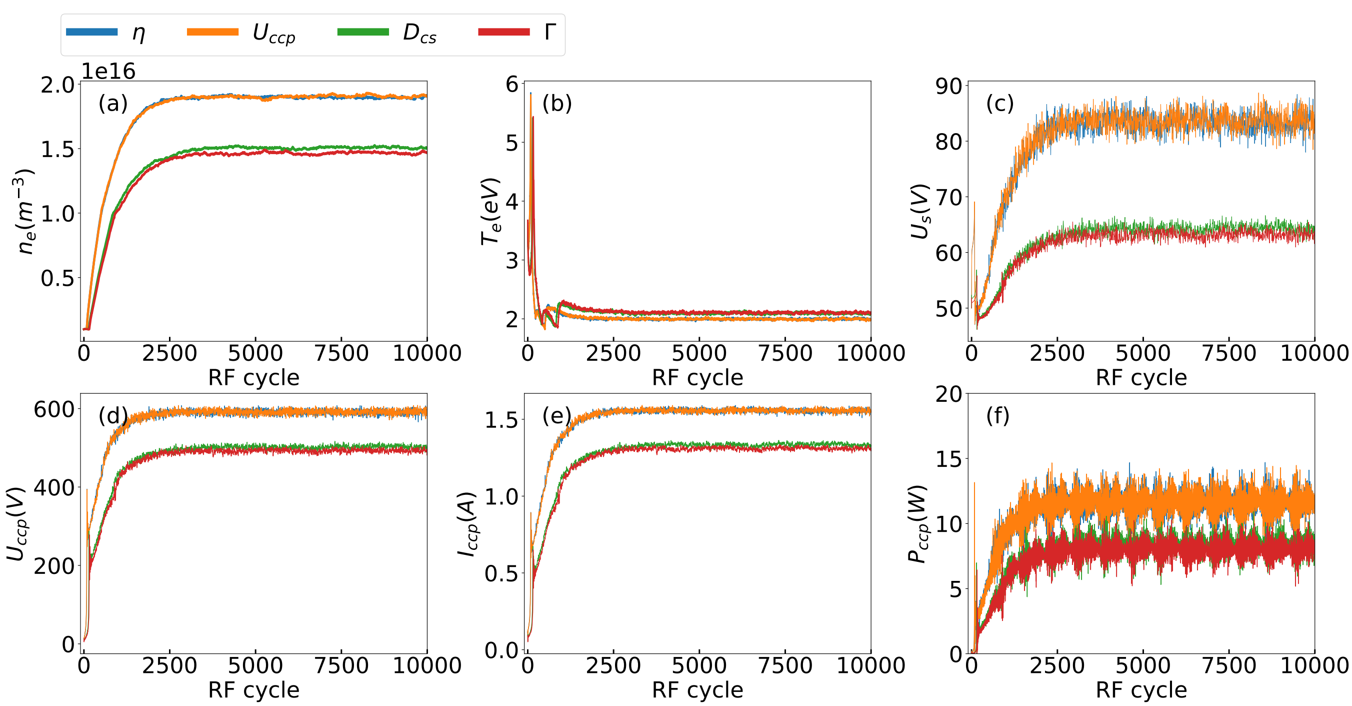

FIG. 10. Comparison of the spatiotemporal evolution of the optimization results corresponding to different optimization objectives. (a) Electron density. (b) The electron temperature. (c) The potential of the upper electrode. (d) The magnitude of the plasma load voltage. (e) The magnitude of the plasma load current. (f) Plasma load power absorption.

such as current, voltage, and power.

$$U_{0,new} = U_{0,old} + \alpha \left(\frac{P_{set} - P_{actual}}{P_{set}} \right), \tag{12}$$

where $U_{0,new}$ is the voltage amplitude after feedback control, $U_{0,old}$ is the voltage amplitude before feedback control, P_{set} is the set power value, and P_{actual} is the actual power value, the speed of feedback adjustment can be controlled by changing α, here we set it to 10.0.

TABLE IV. The best matching parameters obtained under different optimization objectives.

target	C_{m1}(pF)	C_{m2}(pF)	$L(\mu$H)
η	286.027	200	5.726
U_{ccp}	286.833	200	5.723
D_{cs}	444.667	200	5.507
$\|\Gamma\|$	469.444	200	5.495
Yu[a]	461.900	200	5.560

[a] The best matching parameter combination given in Yu's paper using numerical iterative methods, the optimization direction chosen in his paper is to minimize $|\Gamma|$.

TABLE V. The optimization parameter values corresponding to different optimization targets.[a]

target	η	$Uccp(V)$	D_{CS}	$\|\Gamma\|$
η	57.87%	590.67	0.35075	0.48066
U_{ccp}	58.09%	591.62	0.36012	0.47065
D_{cs}	41.67%	502.98	0.85778	0.07692
$\|\Gamma\|$	40.13%	492.51	0.88930	0.07689

[a] All the data here is obtained under stable state.

TABLE VI. The values of plasma parameters and circuit parameters corresponding to different optimization targets.[a]

target	$n_e(m^{-3})$	$T_e(eV)$	$P_s(W)$[b]	$P_{IMN}(W)$[c]	$P_{CCP}(W)$[d]
η	$1.90 * 10^{16}$	1.99	20	2.63	11.58
U_{ccp}	$1.91 * 10^{16}$	1.99	20	2.62	11.63
D_{cs}	$1.51 * 10^{16}$	2.09	20	1.92	8.34
$\|\Gamma\|$	$1.47 * 10^{16}$	2.11	20	1.84	8.03

[a] All the data here is obtained under stable state.
[b] The power output from the power source.
[c] The power dissipated in the Impedance Matching Network (IMN).
[d] The power absorbed by the plasma load.

It is easy to see that the results optimized for absorption efficiency and CCP load voltage are basically the same, while the results optimized for reflection coefficient and impedance similarity are basically the same. In comparison, plasma performance with respect to absorption efficiency and CCP load voltage optimization is superior, exhibiting higher electron density and absorption power. However, it should be noted that the corresponding modulus of the reflection coefficient is relatively large, reaching nearly 0.5. On the other hand, the optimization results targeting impedance matching, while not achieving as high electron density and absorption power, lead to a significantly smaller modulus of the reflection coefficient. This suggests that obtaining high electron density comes at the expense of generating a higher degree of power reflection. Therefore, if ensuring a sufficiently low level of power reflection is crucial in practical applications, then the two matching objectives based on impedance matching should be chosen. However, if there are no restrictions on reflection power and only high electron density and plasma load voltage are required, then optimization based on absorption efficiency and load voltage should be given greater consideration.

Regarding Table V, we should note that there are cases where different optimization objectives converge to the same region. As mentioned in Sec.III A 1, results within the same region are very close. This leads to what is shown in the table: When optimizing for absorption efficiency, the achieved efficiency is slightly lower than that obtained when optimizing for plasmaload voltage. Similarly, when optimizing for impedance similarity, the achieved impedance similarity is slightly lower than that achieved when optimizing for the reflection coefficient. In such cases, as long as the results are close, it is considered normal due to the convergence of optimization regions.

IV. CONCLUSIONS

In this paper, we propose a machine learning-based approach to optimize impedance matching in CCP systems. The proposed method utilizes ANN as a surrogate model to effectively depict the matching performance. The ANN is trained on a dataset of simulated circuit responses and can then be used to predict the matching performance for different combinations of component values. This allows for efficient exploration of the vast parameter space, and can be used to find optimal component values that minimize reflected power and maximize power transfer efficiency.

This paper first provides a detailed introduction to the optimization process with the modulus of the reflection coefficient as the objective. It demonstrates that our method can yield a correct and reliable optimization direction, and ultimately, we can identify a parameter region that meets the requirements and exhibits similar performance. Additionally, by comparing the optimization results based on four different parameters, namely plasma load power absorption efficiency, voltage at both ends of the load, impedance similarity between the power source and the load, and magnitude of the reflection coefficient at the load, we outline the advantages and disadvantages of each optimization parameter. Furthermore, we provide recommendations on which parameters to choose under specific circumstances.

The proposed method has several advantages over traditional methods for optimizing impedance matching in CCP systems. First, the ANN can be used to efficiently explore the vast parameter space, which can significantly reduce the time required to find optimal component values. Second, the ANN is a nonparametric model, which means that it does not make any assumptions about the underlying relationship between the input and output variables. This makes the ANN more robust to changes in the system and allows it to be used to predict the matching performance for a wider range of component values.

However, there are some limitations to the proposed method. First, it is a time-consuming step to perform parameter scanning to obtain training data. Second, the proposed method is still under development, and more work is needed to improve its accuracy and robustness.

Note that although this paper only investigates the combination of C_{m1} and L, ANN itself is an $'$n to n$'$ method, so theoretically it is possible to explore multiple parameter combinations simultaneously. However, the larger the combination of parameters, the longer it takes to obtain the data and train the model. Additionally, as ML is a data-driven method, it can directly fit and optimize the experimental data. In our future work, we will use experimental data for optimization and compare it with the results of numerical simulations.

In conclusion, consistent parameter performance within the identified region highlights the robustness and stability of the system. Even if the values of the specific parameters vary slightly due to inherent uncertainties or fluctuations in operating conditions, the overall performance remains reliable and satisfactory. This robustness in the face of variations is crucial for industrial applications where maintaining stable and predictable outcomes is critical. Additionally, due to the advantages of machine learning in large parameter spaces, this method is ultimately easy to expand to more complex cases such as dual frequency and pulsed CCP.

ACKNOWLEDGMENTS

This work was supported by the National Natural Science Foundation of China (11975174, 12275095 and 12011530142).

ORCIDS

Shimin Yu https://orcid.org/0000-0002-3832-5252
Zili Chen https://orcid.org/0000-0002-2104-5369
Yu Wang https://orcid.org/0000-0003-3519-3677
Zhipeng Chen https://orcid.org/0000-0002-8330-0070
Wei Jiang https://orcid.org/0000-0002-9394-585X
Ya Zhang https://orcid.org/0000-0003-0473-467X

DATA AVAILABILITY STATEMENT

The data that support the findings of this study are available from the corresponding author upon reasonable request.

CONFLICT OF INTEREST

The authors have no conflicts to disclose.

[1] S. Sharma, N. Sirse, A. Kuley, and M. M. Turner, "Plasma asymmetry and electron and ion energy distribution function in capacitive discharges excited by tailored waveforms," Journal of Physics D: Applied Physics **55**, 275202 (2022).

[2] J. W. Coburn and H. F. Winters, "Plasma etching - A discussion of mechanisms," Journal of Vacuum Science and Technology **16**, 391–403 (1979), https://pubs.aip.org/avs/jvst/article-pdf/16/2/391/11825372/391_1_online.pdf.

[3] M. Wang and M. J. Kushner, "High energy electron fluxes in dc-augmented capacitively coupled plasmas. II. Effects on twisting in high aspect ratio etching of dielectrics," Journal of Applied Physics **107**, 023309 (2010), https://pubs.aip.org/aip/jap/article-pdf/doi/10.1063/1.3290873/13057466/023309_1_online.pdf.

[4] H. Zhang, J. Xu, and G. Wang, "Fundamental study on plasma deposition manufacturing," Surface and Coatings Technology **171**, 112–118 (2003).

[5] D. P. Thanu, E. S. Srinadhu, M. Zhao, N. V. Dole, and M. Keswani, "Chapter 8 - fundamentals and applications of plasma cleaning," in *Developments in Surface Contamination and Cleaning: Applications of Cleaning Techniques*, edited by R. Kohli and K. Mittal (Elsevier, 2019) pp. 289–353.

[6] E. Liston, L. Martinu, and M. Wertheimer, "Plasma surface modification of polymers for improved adhesion: a critical review," Journal of Adhesion Science and Technology **7**, 1091–1127 (1993), https://doi.org/10.1163/156856193X00600.

[7] V. Parro and F. Pait, "An automatic impedance matching system for a multi point power delivery continuous industrial microwave oven," in *Proceedings of the 2004 IEEE International Conference on Control Applications, 2004.*, Vol. 1 (2004) pp. 143–148 Vol.1.

[8] C. Qu, S. J. Lanham, S. C. Shannon, S. K. Nam, and M. J. Kushner, "Power matching to pulsed inductively coupled plasmas," Journal of Applied Physics **127**, 133302 (2020), https://pubs.aip.org/aip/jap/article-pdf/doi/10.1063/5.0002522/14769500/133302_1_online.pdf.

[9] F. Schmidt, J. Schulze, E. Johnson, J.-P. Booth, D. Keil, D. M. French, J. Trieschmann, and T. Mussenbrock, "Multi frequency matching for voltage waveform tailoring," Plasma Sources Science and Technology **27**, 095012 (2018).

[10] J. Franek, S. Brandt, B. Berger, M. Liese, M. Barthel, E. Schüngel, and J. Schulze, "Power supply and impedance matching to drive technological radio-frequency plasmas with customized voltage waveforms," Review of Scientific Instruments **86**, 053504 (2015), https://pubs.aip.org/aip/rsi/article-pdf/doi/10.1063/1.4921399/13362444/053504_1_online.pdf.

[11] J. Poulose, M. Goeckner, S. Shannon, D. Coumou, and L. Overzet, "Driving frequency fluctuations in pulsed capacitively coupled plasmas," The European Physical Journal D **71**, 1–12 (2017).

[12] J. Lee and S. Hong, "Dual-frequency rf impedance matching circuits for semiconductor plasma etch equipment," Electronics **10** (2021), 10.3390/electronics10172074.

[13] C. Yang, K. Jin, D. Mao, and X. Zhu, "Precise configuration of transmission line class-e power amplifier operating at ghz frequency," IEEE Journal of Emerging and Selected Topics in Power Electronics **10**, 6396–6404 (2022).

[14] R. Sinha and A. De, "Theory on matching network in viewpoint of transmission phase shift," IEEE Transactions on Microwave Theory and Techniques **64**, 1704–1716 (2016).

[15] C. Zhang and R. Ordóñez, "Impedance matching in semiconductor plasma processing chamber," in *Extremum-Seeking Control and Applications: A Numerical Optimization-Based Approach* (Springer London, London, 2012) pp. 133–153.

[16] L. Zhou and D. Li, "Numerical simulation of icp source impedance and experimental verification," in *2020 IEEE 1st China International Youth Conference on Electrical Engineering (CIYCEE)* (2020) pp. 1–5.

[17] Z. V. Missen, S. Macheret, A. Semnani, and D. Peroulis, "Plasma switch-based technology for high-speed and high-power impedance tuning," in *2021 IEEE 21st Annual Wireless and Microwave Technology Conference (WAMICON)* (2021) pp. 1–4.

[18] I. Adamovich, S. Agarwal, E. Ahedo, L. L. Alves, S. Baalrud, N. Babaeva, A. Bogaerts, A. Bourdon, P. Bruggeman, C. Canal, *et al.*, "The 2022 plasma roadmap: low temperature plasma science and technology," Journal of Physics D: Applied Physics **55**, 373001 (2022).

[19] M. Kambara, S. Kawaguchi, H. J. Lee, K. Ikuse, S. Hamaguchi, T. Ohmori, and K. Ishikawa, "Science-based, data-driven developments in plasma processing for material synthesis and device-integration technologies," Japanese Journal of Applied Physics **62**, SA0803 (2022).

[20] S. Rauf and M. J. Kushner, "The effect of radio frequency plasma processing reactor circuitry on plasma characteristics," Journal of Applied Physics **83**, 5087–5094 (1998), https://pubs.aip.org/aip/jap/article-pdf/83/10/5087/10589503/5087_1_online.pdf.

[21] S. Rauf, "Dual radio frequency sources in a magnetized capacitively coupled plasma discharge," IEEE Transactions on Plasma Science **31**, 471–478 (2003).

[22] M. M. Salem, J.-F. Loiseau, and B. Held, "Impedance matching for optimization of power transfer in a capacitively excited rf plasma reactor," The European Physical Journal-Applied Physics **3**, 91–95 (1998).

[23] S. Yu, Z. Chen, H. Wu, L. Guo, Z. Wang, W. Jiang, and Y. Zhang, "Best impedance matching seeking of single-frequency capacitively coupled plasmas by numerical simulations," Journal of Applied Physics **132**, 083302 (2022), https://doi.org/10.1063/5.0096910.

[24] A. D. Bonzanini, K. Shao, D. B. Graves, S. Hamaguchi, and A. Mesbah, "Foundations of machine learning for low-temperature plasmas: methods and case studies," Plasma Sources Science and Technology **32**, 024003 (2023).

[25] J. Trieschmann, L. Vialetto, and T. Gergs, "Machine learning for advancing low-temperature plasma modeling and simulation," arXiv preprint arXiv:2307.00131 (2023).

[26] K. J. Kanarik, W. T. Osowiecki, Y. Lu, D. Talukder, N. Roschewsky, S. N. Park, M. Kamon, D. M. Fried, and R. A. Gottscho, "Human–machine collaboration for improving semiconductor process development," Nature **616**, 707–711 (2023).

[27] R. Shadmehr, D. Angell, P. B. Chou, G. S. Oehrlein, and R. S. Jaffe, "Principal component analysis of optical emission spectroscopy and mass spectrometry: Application to reactive ion etch process parameter estimation using neural networks," Journal of The Electrochemical Society **139**, 907 (1992).

[28] S. J. Hong, G. May, and D.-C. Park, "Neural network modeling of reactive ion etching using optical emission spectroscopy data," IEEE Transactions on Semiconductor Manufacturing **16**, 598–608 (2003).

[29] C. Himmel and G. May, "Advantages of plasma etch modeling using neural networks over statistical techniques," IEEE Transactions on Semiconductor Manufacturing **6**, 103–111 (1993).

[30] A. Bleakie and D. Djurdjanovic, "Growing structure multiple model system for quality estimation in manufacturing processes," IEEE Transactions on Semiconductor Manufacturing **29**, 79–97 (2016).

[31] T. Gergs, T. Mussenbrock, and J. Trieschmann, "Physics-separating artificial neural networks for predicting initial stages of al sputtering and thin film deposition in ar plasma discharges," Journal of Physics D: Applied Physics **56**, 084003 (2023).

[32] X.-C. Wang and Y.-T. Zhang, "Modeling of discharge characteristics and plasma chemistry in atmospheric co2 pulsed plasmas employing deep neural network," Journal of Applied Physics **133** (2023).

[33] Y.-T. Zhang, S.-H. Gao, and Y.-Y. Zhu, "Efficient numerical simulation on dielectric barrier discharges at atmospheric pressure integrated by deep neural network," Journal of Applied Physics **133** (2023).

[34] J. Brackbill and D. Forslund, "An implicit method for electromagnetic plasma simulation in two dimensions," Journal of Computational Physics **46**, 271–308 (1982).

[35] B. I. Cohen, A. Langdon, and A. Friedman, "Implicit time integration for plasma simulation," Journal of Computational Physics **46**, 15–38 (1982).

[36] H. yu Wang, W. Jiang, and Y. nian Wang, "Implicit and electrostatic particle-in-cell/monte carlo model in two-dimensional and axisymmetric geometry: I. analysis of numerical techniques," Plasma Sources Science and Technology **19**, 045023 (2010).

[37] H. Wu, Y. Zhou, J. Gao, Y. Peng, Z. Wang, and W. Jiang, "Electrical breakdown in dual-frequency capacitively coupled plasma: a collective simulation," Plasma Sources Science and Technology **30**, 065029 (2021).

[38] M. M. Turner, A. Derzsi, Z. Donkó, D. Eremin, S. J. Kelly, T. Lafleur, and T. Mussenbrock, "Simulation benchmarks for low-pressure plasmas: Capacitive discharges," Physics of Plasmas **20**, 013507 (2013), https://pubs.aip.org/aip/pop/article-pdf/doi/10.1063/1.4775084/13430854/013507_1_online.pdf.

[39] D.-Q. Wen, J. Krek, J. T. Gudmundsson, E. Kawamura, M. A. Lieberman, P. Zhang, and J. P. Verboncoeur, "On the importance of excited state species in low pressure capacitively coupled plasma argon discharges," Plasma Sources Science and Technology **32**, 064001 (2023).

[40] M. Roberto, H. Smith, and J. Verboncoeur, "Influence of metastable atoms in radio-frequency argon discharges," IEEE Transactions on Plasma Science **31**, 1292–1298 (2003).

[41] L. Lauro-Taroni, M. M. Turner, and N. S. Braithwaite, "Analysis of the excited argon atoms in the gec rf reference cell by means of one-dimensional pic simulations," Journal of Physics D: Applied Physics **37**, 2216 (2004).

[42] L. Wang, P. Hartmann, Z. Donkó, Y.-H. Song, and J. Schulze, "Effects of structured electrodes on electron power absorption and plasma uniformity in capacitive RF discharges," Journal of Vacuum Science & Technology A **39**, 063004 (2021), https://pubs.aip.org/avs/jva/article-pdf/doi/10.1116/6.0001327/15934134/063004_1_online.pdf.

[43] B. Zheng, Y. Fu, D. qi Wen, K. Wang, T. Schuelke, and Q. H. Fan, "Influence of metastable atoms in low pressure magnetized radio-frequency argon discharges," Journal of Physics D: Applied Physics **53**, 435201 (2020).

[44] Y. Zhang, W. Jiang, Q. Z. Zhang, and A. Bogaerts, "Computational study of plasma sustainability in radio frequency micro-discharges," Journal of Applied Physics **115**, 193301 (2014), https://pubs.aip.org/aip/jap/article-pdf/doi/10.1063/1.4878161/15136150/193301_1_online.pdf.

[45] Y. Zhang, J.-l. Huang, L. Yi, H.-y. Wang, and W. Jiang, "Electron energy probability function modulation with external electron beam in capacitive coupled radio frequency discharges," Plasma Processes and Polymers **15**, 1700169 (2018), https://onlinelibrary.wiley.com/doi/pdf/10.1002/ppap.201700169.

[46] W. Jiang, H. yu Wang, Z. hua Bi, and Y. nian Wang, "Implicit and electrostatic particle-in-cell/monte carlo model in two-dimensional and axisymmetric geometry: Ii. self-bias voltage effects in capacitively coupled plasmas," Plasma Sources Science and Technology **20**, 035013 (2011).

[47] M. A. Furman and M. T. F. Pivi, "Probabilistic model for the simulation of secondary electron emission," Phys. Rev. ST Accel. Beams **5**, 124404 (2002).

[48] A. V. Phelps and Z. L. Petrovic, "Cold-cathode discharges and breakdown in argon: surface and gas phase production of secondary electrons," Plasma Sources Science and Technology **8**, R21 (1999).

[49] M. Thompson and J. Fidler, "Determination of the impedance matching domain of impedance matching networks," IEEE Transactions on Circuits and Systems I: Regular Papers **51**, 2098–2106 (2004).

[50] M. Vass, S. Wilczek, T. Lafleur, R. P. Brinkmann, Z. Donkó, and J. Schulze, "Electron power absorption in low pressure capacitively coupled electronegative oxygen radio frequency plasmas," Plasma Sources Science and Technology **29**, 025019 (2020).

[51] O. O. Abegunde, E. T. Akinlabi, O. P. Oladijo, S. Akinlabi, and A. U. Ude, "Overview of thin film deposition techniques," AIMS Materials Science **6**, 174–199 (2019).

[52] A. Agarwal and M. J. Kushner, "Effect of nonsinusoidal bias waveforms on ion energy distributions and fluorocarbon plasma etch selectivity," Journal of Vacuum Science & Technology A **23**, 1440–1449 (2005), https://pubs.aip.org/avs/jva/article-pdf/23/5/1440/13518831/1440_1_online.pdf.

[53] P. Chu, J. Chen, L. Wang, and N. Huang, "Plasma-surface modification of biomaterials," Materials Science and Engineering: R: Reports **36**, 143–206 (2002).

[54] Github repository: https://github.com/hyperopt/hyperopt.